RSC Advances

PAPER

View Article Online
View Journal | View Issue

Cite this: *RSC Adv.*, 2017, **7**, 20451

Facile synthesis of spinel $Cu_{1.5}Mn_{1.5}O_4$ microspheres with high activity for the catalytic combustion of diesel soot†

H. Zhao,[ab] X. X. Zhou,[a] L. Y. Pan,[ab] M. Wang,[ab] H. R. Chen *[ac] and J. L. Shi[ac]

Received 16th February 2017
Accepted 4th April 2017

DOI: 10.1039/c7ra01971h

rsc.li/rsc-advances

A series of Cu–Mn mixed oxides were prepared *via* a facile co-precipitation method and used as catalysts for diesel soot combustion in $NO_x/O_2/N_2$. It is found that the chemical composition in the Cu–Mn mixed oxides has a significant influence on both morphology and catalytic activity. When the Cu/Mn atomic ratio was optimized to be 1, a distinctive pure spinel phase of $Cu_{1.5}Mn_{1.5}O_4$ was obtained (named Cu1Mn1), which exhibited superior catalytic activity (*e.g.*, finishing combustion temperature (T_f) = 360 °C, in loose contact mode). The excellent catalytic activity of Cu1Mn1 was mainly attributed to the following aspects: (1) distinct morphological features: the well-dispersed Cu1Mn1 microspheres with a rough surface could contact soot particles sufficiently, and the stacked pores between the loosely packed nanoparticles within the microspheres could facilitate the diffusion of gaseous O_2, NO and NO_2; and (2) the high intrinsic activity of the $Cu_{1.5}Mn_{1.5}O_4$ phase: the abundant adsorbed oxygen species (O_{ads}) is beneficial to the direct oxidation of soot into CO_2, and the enormous Cu^+–$Mn^{\lambda+}$ (λ = 3, 4, hereinafter inclusive) cation pairs could facilitate the production of the strong oxidant NO_2, and the interaction between Cu^{2+} and NO_2 would lead to high enhancement efficiency of NO_2 for soot combustion. This facile strategy for the high activity spinel phase towards catalytic soot combustion shows great promise for practical applications.

Introduction

The diesel particulate filter (DPF) has been developed for many years as an effective device to trap over 90% of diesel soot, which would otherwise lead to a rise in PM2.5 and thus serious health problems in human beings.[1,2] DPF with trapped soot is usually regenerated in a positive way, such as fuel post-injection, which is applied to increase the exhaust temperature (usually below 400 °C) up to the soot ignition temperature (~600 °C).[3,4] But there remain several limitations for industrial application, such as fuel overconsumption and thermal damage to the filter. Hence, reforming of DPF with a catalyst coating has been proposed to reduce the ignition temperature of the trapped soot. Many kinds of catalysts have been proposed and investigated, *e.g.* the noble metals,[5] transition metal oxides,[6] perovskite and/or perovskite-like mixed oxides,[7] spinel mixed oxides,[8] alkaline/alkaline-earth metal oxides,[9] ceria-based oxides,[10] *etc.* Thereinto, noble metal-based catalysts with a three-dimensional ordered macroporous (3DOM) support[11] or a cordierite support[12] are among the best candidates with outstanding catalytic performance, which can decrease the T_f of soot combustion to as low as 400 °C. Nevertheless, the high cost and sulfur sensitivity of noble metal,[13,14] would impose a severe restriction on its industrial application.

As one of the promising substitutes for noble metal based catalysts, copper manganese spinel-type mixed oxides have been reported to be well suitable for various catalytic processes, *e.g.*, total oxidation of volatile organic compounds,[15] steam reforming of methanol,[16] water gas shift reaction,[17] and low temperature reduction of NO,[18] demonstrating versatile application potential. The physicochemical properties of these spinel-type compounds mainly depend on the type, charge and distribution in tetrahedral/octahedral sites of the cations.[19] Spinels can be divided into stoichiometric (AB_2O_4) and non-stoichiometric spinels ($A_xB_{3-x}O_4$) types, where A, B stand for two kinds of cations, and the subscripts are the atomic ratio of A, B and O atom. The ion distribution in $A_xB_{3-x}O_4$ is rather complex, *e.g.*,

[a]*State Key Laboratory of High Performance Ceramics and Superfine Microstructure, Shanghai Institute of Ceramics Chinese Academy of Sciences, 1295 Ding-Xi Road, Shanghai 200050, P. R. China. E-mail: hrchen@mail.sic.ac.cn*

[b]*University of Chinese Academy of Sciences, Beijing, 100049, P. R. China*

[c]*Jiangsu National Synergetic Innovation Center for Advanced Materials (SICAM), Nanjing, P. R. China*

† Electronic supplementary information (ESI) available: Characteristic temperatures (T_i, T_m and T_f) and selectivity to CO_2 for catalytic soot combustion over all studied catalysts and non-catalyzed reference; N_2 adsorption/desorption isotherms & pore size distributions of all studied catalysts; specific surface areas, pore volumes and average pore diameters of all studied catalysts; SEM image and corresponding EDS spectrum of Cu1Mn2; SEM image and corresponding EDS spectrum of Cu1Mn1; STEM image of Cu1Mn1; catalytic soot oxidation in O_2/N_2 under loose contact mode over all studied catalysts; catalytic NO oxidation over CuO, Cu1Mn1 and MnO_δ; catalytic soot combustion over CuO, Cu1Mn1 and MnO_δ with or without NO. See DOI: 10.1039/c7ra01971h

$Cu_xMn_{3-x}O_4$ with four kinds of cations, shows a configuration of $[Cu_a{}^{+}Mn_b{}^{2+}Cu_c{}^{2+}Mn_{1-a-b-c}{}^{3+}]_\alpha[Cu_{x-a-c}{}^{2+}Mn_{3-2x-b+c}{}^{3+}Mn_{x+a+b-1}{}^{4+}]_\beta O_4$, where the subscripts except α and β are for the atomic ratios of the ions in specific sites.[20] When x in $Cu_xMn_{3-x}O_4$ is adjusted, different structural, electrical or magnetic properties can be realized. For example, $Cu_{1.5}Mn_{1.5}O_4$ ($[Cu^+]_\alpha[Cu_{0.5}{}^{2+}Mn_{1.5}{}^{4+}]_\beta O_4$) contains abundant Cu^+ and Mn^{4+} cations (arising from reaction (1)),[21,22] which are respectively stabilized in the tetrahedral and octahedral sites without the need of a stabilizing agent.[20] This $Cu_{1.5}Mn_{1.5}O_4$ phase is expected to be much beneficial for diesel soot combustion, since the high concentration of Cu^+ and Mn^{4+} cations could activate O_2 and NO_x in the diesel exhaust, respectively, thus facilitating NO_2 production.

$$Cu^{2+} + Mn^{3+} \rightarrow Cu^{+} + Mn^{4+} \quad (1)$$

Our previous work confirmed that the spinel $Cu_{1.5}Mn_{1.5}O_4$ loaded on zeolite beta could exhibit excellent activity for catalytic soot combustion, which was partially attributed to the synergetic catalytic effect between the valence-changeable cooper and manganese cations within the spinel phase.[23] However, there still remain several drawbacks, such as complexity in preparation and the limited loading amount of active spinel $Cu_{1.5}Mn_{1.5}O_4$. In this work, a facial, scalable and environmentally-friendly co-precipitation method was utilized to prepare a series of Cu–Mn mixed oxides with different Cu/Mn atomic ratios as catalysts for soot combustion. Thereinto, Cu1Mn1 (atomic ratio of Cu : Mn equals to 1 : 1) with a pure spinel $Cu_{1.5}Mn_{1.5}O_4$ phase exhibits the best activity, showing a much low T_f value of 360 °C even compared to the reported 400 °C.[11,12] Multiple measurements have been conducted to reveal the reason for the high activity of $Cu_{1.5}Mn_{1.5}O_4$ phase. A plausible mechanism for soot combustion over Cu1Mn1 is also proposed.

Experimental

Catalyst preparation

All the chemicals used in this study were of analytical grade, and were used without further purification. Cu–Mn mixed oxides were prepared by the co-precipitation method as reported before with some modification.[24] The whole procedure was performed at room temperature expect the drying and calcination steps. A typical preparation procedure was as follows: firstly, 7.5 mmol of nitrates including $Cu(NO_3)_2\cdot 3H_2O$ and $Mn(NO_3)_2$ (50 wt% in aqueous solution) with different Cu/Mn atomic ratios were thoroughly dissolved in 30 mL of deionized water under stirring. Then, another 30 mL of deionized water with 30 mmol of $NaHCO_3$ dissolved in it was quickly poured into the nitrate solution and was left to react for 30 min with the pH of the solution reaching a final value of 8–9. The precipitates were centrifuged and rinsed thoroughly with deionized water and absolute ethyl alcohol alternately for several times until the residual Na content in the supernatant was below 0.5 wt% (measured by inductively coupled plasma-atomic emission spectrometry, ICP-AES). After drying at 100 °C, the as-prepared samples were grinded and then calcined under static air at 500 °C for 2 h with a heating rate of 1 °C min^{-1}. For ease of reference, the prepared catalysts are designated CuxMny, where $x : y$ stands for the Cu : Mn atomic ratio in the recipe. In addition, single oxide CuO or MnO_δ for reference was also prepared with the same synthesis procedure in the absence of $Mn(NO_3)_2$ or $Cu(NO_3)_2\cdot 3H_2O$.

Characterizations

Powder X-ray diffraction (XRD) patterns of the prepared samples were obtained using a Rigaku D/Max 2200 PC diffractometer with Cu Kα radiation (40 kV and 40 mA). The nitrogen adsorption and desorption curves were recorded using Micromeritics Tristar 3000 at 77 K, and the specific surface area (SSA) and the pore size distribution were calculated using the Brunauer–Emmett–Teller (BET) and Barrett–Joyner–Halenda (BJH) methods, respectively. Scanning transmission electron microscopic (STEM) and elements mapping imaging were performed using Hitachi S-4800. X-ray photoelectron spectroscopy (XPS) signals were recorded using an ESCAlab250 instrument. The fitting of the Mn element was carried out using Gaussian fitting parameters. The diffuse reflectance infrared Fourier transform (DRIFT) spectra were obtained at different temperatures in the range of RT-400 °C, using a Thermo-Scientific Nicolet FT-IR model iS10 equipped with an *in situ* DRIFTS cell (Harric Scientific Inc.) and a gas flow system. The pre-mixed catalyst/soot (mass ratio = 10 : 1, in total of 3 mg) was diluted with KBr powder (80 mg) and then filled into the DRIFTS cell. The DRIFTS cell was then exposed to certain reactant gas mixtures (350 ppm NO, 10% O_2, and N_2 as balance, total flow = 200 mL min^{-1}), and the spectra were recorded after the temperature was stable for 20 min for each temperature. The temperature-programed reduction with hydrogen (H_2-TPR) experiments were performed using a Micromeritics Chemisorb 2750 instrument in a 5% H_2/N_2 flow (25 mL min^{-1}) using 50 mg catalyst with a heating rate of 10 °C min^{-1}. The uptake amount of H_2 was measured using a thermal conductivity detector (TCD). Na content was analyzed by means of ICP-AES.

Catalytic activity measurements

Carbon black from Degussa (Printex U, diameters: 10–50 nm) was used as the model soot particles. Following a well-accepted procedure,[23] the model soot particles (10 mg) and catalyst (100 mg) were carefully mixed for 20 min with a spatula to simulate the loose contact mode. Then, the mixture was loaded in a quartz tube (i.d. 6.0 mm), after mixing with 1 g silica pellets to avoid pressure drop and favor heat transfer. A gas mixture of 350 ppm NO, 10% O_2 and balance N_2 was feed with a flow rate of 200 mL min^{-1}, leaving the space velocity to be 120 000 mL g^{-1} h^{-1}. The mixture was then heated at a rate of 5 °C min^{-1} in a tube furnace equipped with a thermal couple. To minish the error of the measurement to a least extent, every gas flow was confirmed by a mechanical gas flowmeter and the concentration of NO_x was verified by a NO_x analyzer (Thermo Fisher 42i-LS). The analysis of the emissions from the reactor was performed using an online GC-FID analyzer equipped with a methane converter. The catalytic activities (conversion and

selectivity) were calculated as indicated in previous reports in the literature,[10,25] in terms of T_i, T_m and T_f, which were defined as the temperatures at 10%, 50% and 90% of soot conversion, respectively, as well as the selectivity to CO_2 (S_{CO_2}), which was defined as the integrated CO_2 outlet amount divided by integrated CO_x (containing CO and CO_2) outlet amount during the whole combustion process. For the repeated activity tests, the spent catalyst, still mixed with silica pellets, was recharged with fresh soot particles (10 mg), followed by a thorough mixing using a spatula to simulate the loose soot–catalyst contact. Following the identical procedure to that described above, the activity tests were repeated 5 times.

Results and discussion

Soot combustion catalytic activity

Fig. 1a shows the catalytic activities of different Cu*x*Mn*y* catalysts and reference CuO and MnO_δ towards soot combustion in $NO_x/O_2/N_2$ (catalyst–soot in loose contact mode). It is clear that all the catalysts can greatly promote soot combustion, and improve the selectivity to CO_2 formation from ~60% to over 90% (Table S1†). Especially, Cu1Mn1 exhibits the best catalytic activity with the lowest characteristic temperatures (temperature of maximum soot combustion rate (T_m) = 330 °C, and T_f = 360 °C), which are desirably within the temperature range of diesel exhaust (175–400 °C).[3] Additionally, it is worth noting that both Cu2Mn1 and Cu1Mn2 show lower catalytic activity than CuO, indicating that suitable Cu/Mn ratio (1 : 1 in this case), which could lead to a strong synergetic effect, is crucial to the enhanced catalytic activity. Moreover, the reusability of the optimized Cu1Mn1 is observed to be of excellence (Fig. S1†), with T_f and T_m below 380 and 370 °C, respectively, even after 5 runs of repeated catalytic soot combustion tests. It should be noted that the slight loss of catalytic activity in repeated tests could be mainly attributed to the inevitable catalyst mass loss. Additionally, the selectivity of CO_2 was kept ~95% in the repeated tests, also demonstrating the stable and excellent catalytic activity. The effect of the residual Na species in Cu1Mn1 on the catalytic activity for soot combustion has also been investigated. As shown in Fig. S2 and S3,† the residual Na species (0.32 wt% by ICP-AES) impose no obvious influences on the catalytic activity of the spinel $Cu_{1.5}Mn_{1.5}O_4$ phase.

To get a kinetics insight into the catalytic soot combustion over CuO, Cu*x*Mn*y* and MnO_δ, the corresponding Arrhenius curves (Fig. 1b) were plotted from the CO_x concentration–temperature curves shown in Fig. S4† using an integral method.[26] The kinetics parameters, such as apparent activation energy (E_a) and frequency factor (A) are derived from the Arrhenius plots and summarized in Table 1, according to the Arrhenius equation: $\ln k = \ln A - E_a/RT$, where k is specific reaction rate, R is molar gas constant, T is temperature in Kelvin. As can be seen in Table 1, the value of E_a gradually decreases with increasing Mn content, reaching the highest in CuO (140.0 kJ mol^{-1}) and the lowest in MnO_δ (48.1 kJ mol^{-1}), while keeping roughly constant in Cu*x*Mn*y* (100–116 kJ mol^{-1}),

Table 1 Apparent activation energy, "ln *A*" values and lattice constant derived from XRD patterns of different catalysts

Catalyst	CuO	Cu2Mn1	Cu1Mn1	Cu1Mn2	MnO_δ
E_a[a] (kJ mol^{-1})	140.0	115.8	115.6	100.7	48.1
ln A[a]	27.37	21.97	23.70	18.49	9.16
Lattice constant[b] (Å)	a = 4.687 b = 3.433 c = 5.134	8.279	8.283	8.266	9.414

[a] Derived from the $\ln k - 1/T$ plots in Fig. 1b according to Arrhenius equation: $\ln k = \ln A - E_a/RT$. [b] Derived from XRD patterns shown in Fig. 2.

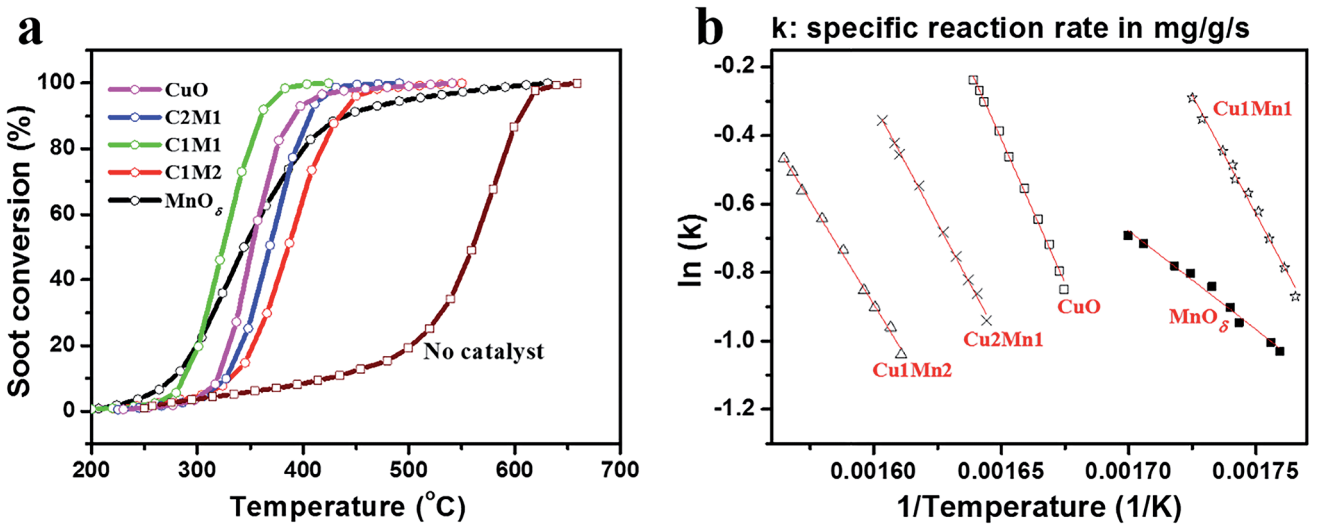

Fig. 1 Soot combustion performance without catalyst, or with different catalysts under loose contact mode (a), and the corresponding Arrhenius plots (b) (reaction conditions: 350 ppm NO and 10% O_2 in N_2 with a total flow of 200 mL min^{-1}, mass of soot–catalyst–silica is 10–100–1000 mg).

indicating the similar catalysis mechanism for soot combustion over Cu*x*Mn*y*. Additionally, as shown in Table 1, CuO and Cu1Mn1 show higher (ln *A*) values among all the catalysts, while MnO_δ possesses the lowest one. Therefore, according to the Arrhenius equation, it can be inferred that Cu1Mn1 could show the best catalytic activity, as confirmed in Fig. 1b, where Cu1Mn1 can achieve high (ln *k*) value even at the largest 1/*T* (*i.e.*, the lowest temperature). More detailed characterizations were conducted and analyzed as follows.

Physical and textural properties

The XRD patterns of different Cu*x*Mn*y* oxides and reference MnO_δ and CuO are displayed in Fig. 2, and the corresponding lattice constant data are listed in Table 1. Apparently, all the samples show well crystallization. Thereinto, CuO presents pure phase of monoclinic CuO, while MnO_δ exhibits mixed MnO_2–Mn_2O_3 phases, suggesting the co-existence of Mn species with different valence states. Interestingly, only Cu1Mn1 possesses pure spinel phase of $Cu_{1.5}Mn_{1.5}O_4$. Whereas, Cu2Mn1 shows a secondary CuO phase besides the predominant spinel $Cu_{1.5}Mn_{1.5}O_4$; and in Cu1Mn2, some amorphous or highly dispersed manganese oxides co-exist with the main spinel $Cu_{1.5}Mn_{1.5}O_4$. More interestingly, it is worth noting that the crystallinity of $Cu_{1.5}Mn_{1.5}O_4$ spinel phase decreases in the order of Cu1Mn1 > Cu2Mn1 > Cu1Mn2, which presents the same tendency with the order of catalytic activity (Fig. 1a). Thus it is reasonable to assume that a well crystalized $Cu_{1.5}Mn_{1.5}O_4$ spinel phase could be mainly responsible for the improved catalytic activity towards soot combustion over Cu*x*Mn*y*. Detailed information about the SSA and pore structure for each catalyst can be found in Fig. S5 and Table S2.† Thereinto, Cu1Mn1 shows the lowest SSA value among Cu*x*Mn*y*, consistent with its highest crystallinity (Fig. 2). Nevertheless, Cu1Mn1 exhibits the highest activity towards catalytic soot combustion, demonstrating the high intrinsic activity of the spinel $Cu_{1.5}Mn_{1.5}O_4$ phase.

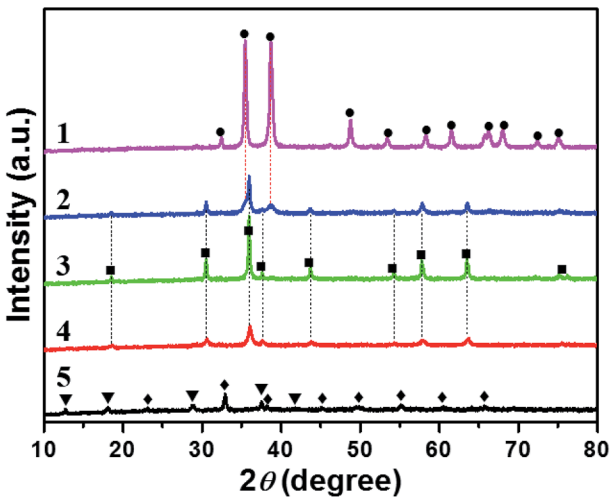

Fig. 2 XRD patterns of different samples, (1) CuO, (2) Cu2Mn1, (3) Cu1Mn1, (4) Cu1Mn2 and (5) MnO_δ. ● CuO (JCPDS 80-1916), ■ $Cu_{1.5}Mn_{1.5}O_4$ (JCPDS 70-0260), ▼ MnO_2 (JCPDS 72-1982), ◆ Mn_2O_3 (JCPDS 73-1826).

Furthermore, the characterization of morphology and chemical composition of these catalysts was conducted for comparison.

Morphology

The different morphology and elemental distribution images of Cu2Mn1, Cu1Mn1 and Cu1Mn2 are depicted in Fig. 3. It is clear that well-dispersed microspheres and nanoparticles co-exist in Cu2Mn1, and the microspheres show uniform distribution of Cu and Mn species while the nanoparticles mainly consist of copper oxide species. Whereas, Cu1Mn2 presents a unique core–shell structure, with uniformly-distributed Cu and Mn species in the core and excessive Mn species in the shell (Fig. S6,† Mn/Cu > 1.3).

Different from either Cu2Mn1 or Cu1Mn2, only homogeneous microspheres occur in Cu1Mn1. Combined with the XRD results in Fig. 2, it can be inferred that the microspheres in Cu2Mn1 and Cu1Mn1, as well as the inner core in Cu1Mn2 all belong to the spinel $Cu_{1.5}Mn_{1.5}O_4$ phase. The typical SEM image and corresponding EDS result of Cu1Mn1 shown in Fig. S7,† confirm that Cu/Mn atomic ratio in Cu1Mn1 is close to 1 : 1, which is in good consistence with the composition of $Cu_{1.5}Mn_{1.5}O_4$ phase. In addition, Cu1Mn1 microspheres present rather rough surface, different from the smooth surface in Cu1Mn2. The STEM image with high magnification of Cu1Mn1 (Fig. S8†) reveals that the microsphere rough surface is derived from the loosely-packed nanoparticles with particle size of around 20–30 nm and the stacked pores within them. Therefore, the following two aspects are believed to mainly contribute to the excellent catalytic activity of Cu1Mn1: (1) the pure $Cu_{1.5}Mn_{1.5}O_4$ phase without extra components (*e.g.*, CuO nanoparticles in Cu2Mn1 and the Mn-rich shell in Cu1Mn2) benefits the sufficient contact between soot and the active sites on catalyst surface, and (2) the well-dispersion and rough surface of Cu1Mn1 microspheres both favor the sufficient contact between catalyst and soot particles, and the presence of stacked pores within the microspheres is also helpful for the diffusion of gaseous reactant or product, such as O_2, NO and NO_2.

Surface composition measured with XPS

The deconvolutions of the O 1s, Mn 2p and Cu 2p spectra of Cu*x*Mn*y* oxides and the reference MnO_δ and/or CuO are shown in Fig. 4. The O 1s spectrum can be well fitted into a main peak located at 529.6–529.7 eV that is assigned to the lattice oxygen, and several peaks with higher binding energies corresponding to different kinds of absorbed oxygen species.[27] The Mn $2p_{3/2}$ XPS spectrum is composed of three peaks, *i.e.*, peaks at 640.4–640.6, 641.7–642.1 and 643.8–644.0 eV corresponding to Mn^{2+}, Mn^{3+} and Mn^{4+}, respectively,[28,29] and a satellite peak at 646.8–648.4 eV belonging to the MnO satellite feature.[30] As for the Cu 2p XPS spectrum, it is clearly found that the Cu*x*Mn*y* mixed oxides show great difference from pure CuO. Cu $2p_{3/2}$ spectrum of CuO exhibits two peaks, *i.e.*, the main one at 932.7 eV corresponding to Cu^+ and another one at 934.0 eV due to Cu^{2+};[31] while the Cu $2p_{3/2}$ spectra of Cu*x*Mn*y* show peaks at much lower binding energies of 930.7–930.8 eV (Cu^+ in $Cu_{1.5}Mn_{1.5}O_4$), and 933.4–933.7 eV (Cu^{2+} in $Cu_{1.5}Mn_{1.5}O_4$).[32] The remarkable

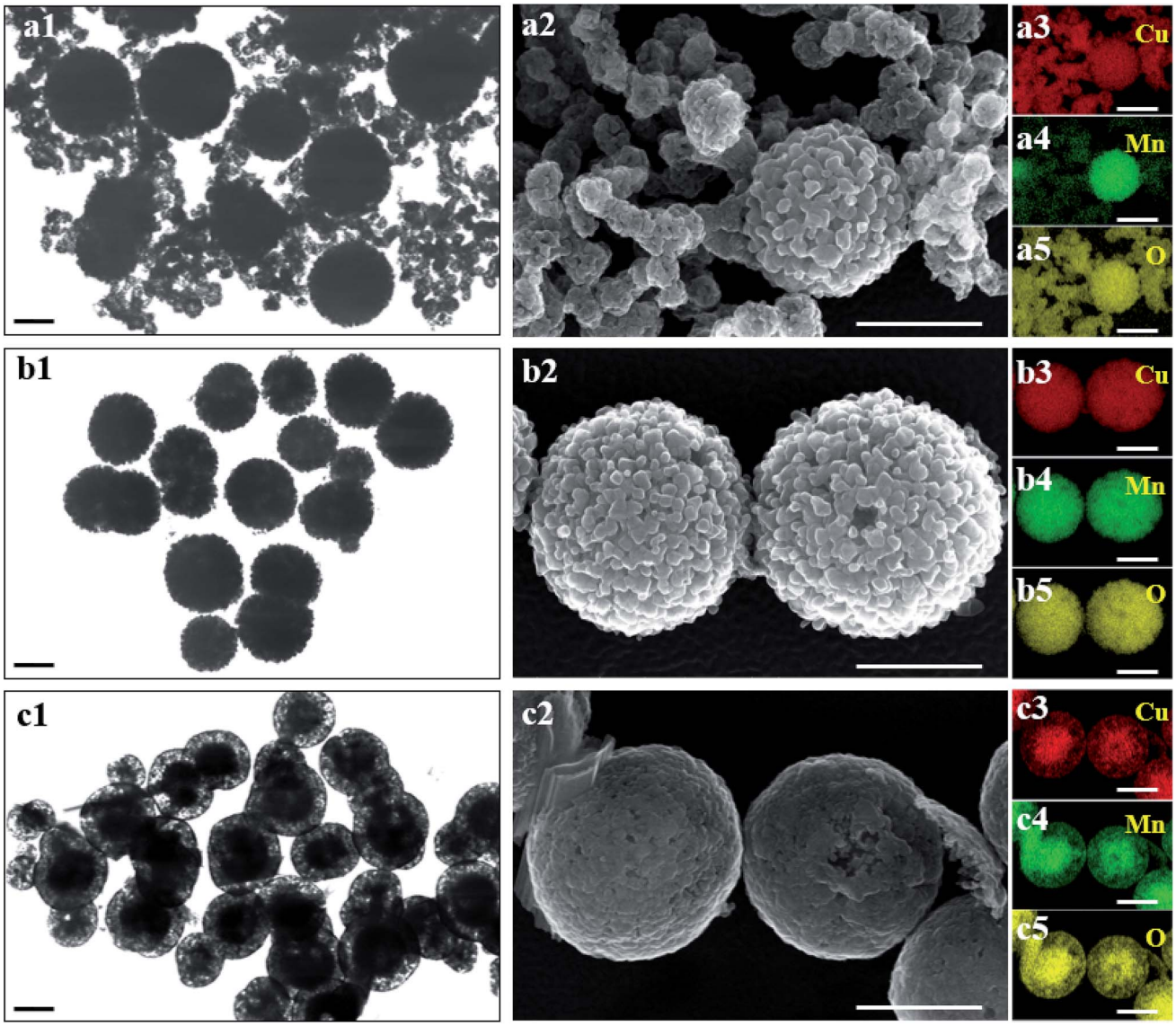

Fig. 3 Typical STEM images (a1, b1, c1), SEM images (a2, b2, c2) and the corresponding elemental mapping (a3–a5, b3–b5, c3–c5) of Cu2Mn1 (a1–a5), Cu1Mn1 (b1–b5) and Cu1Mn2 (c1–c5) samples. Scale bars: 400 nm.

difference in the peak position highlights the great difference in chemical environment between CuO and $Cu_{1.5}Mn_{1.5}O_4$.

Table 2 lists the quantified results of the XPS analysis for Cu*x*Mn*y* oxides, MnO_δ and CuO. It is clearly observed that it is Mn^{3+} instead of Mn^{4+} ($Cu_{1.5}Mn_{1.5}O_4$ = $Cu_{1.0}{}^{+}Cu_{0.5}{}^{2+}Mn_{1.5}{}^{4+}O_4{}^{2-}$), that dominates in the Mn 2p spectra for all the Cu*x*Mn*y* catalysts, confirming the existence of the redox equilibrium ($Cu^+ + Mn^{4+} \leftrightarrow Mn^{3+} + Cu^{2+}$) in the $Cu_{1.5}Mn_{1.5}O_4$ phase.[21,22] As for Cu species, the Cu^+ proportion on catalyst surface rises with increasing Mn content in Cu*x*Mn*y*, reaching a maximum value in Cu1Mn2 (69.6%), which is, however, still lower than that in reference CuO (78.7%). This extremely high Cu^+ proportion in CuO, which can be verified by the rather weak Cu^{2+} satellite peak for CuO in Fig. 4c, corresponds well with its highest ratio of O_{ads}/O (shown in Table 3), since the reduction of Cu^{2+} in CuO is always accompanied by the generation of oxygen vacancies (V_O).[33] The interaction between Cu and Mn species through electron exchange is also verified by H_2-TPR measurement, as shown in Fig. S9,† where H_2 reduction of Cu*x*Mn*y* occurs at much lower temperatures than that for either CuO or MnO_δ. It should be mentioned that there is inconsistence between the activity order and reducibility order, as previously reported,[34] which could be attributed to the difference in chemical and structural properties between H_2 and soot, *e.g.*, reactive species at the inner pores surface can be attacked by H_2 molecule, but are unavailable for soot particles. Nevertheless, H_2-TPR results firmly prove the existence of Cu–Mn synergetic effect in the prepared Cu*x*Mn*y* catalysts.

As reported by previous works, Cu^+–$Mn^{\lambda+}$ cation pair can serve as active site for NO_2 production, since Cu^+ and $Mn^{\lambda+}$ can facilitate the adsorption and activation of O_2 and NO, respectively.[35,36] Therefore a parameter "Ω" was introduced (defined in

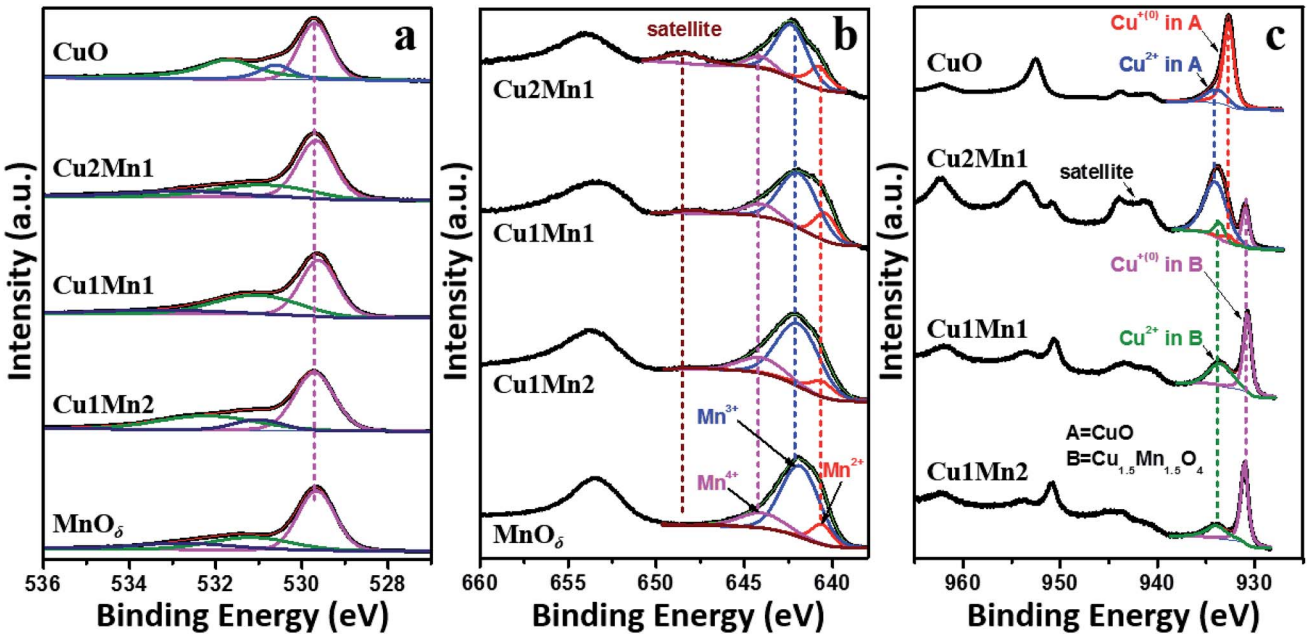

Fig. 4 The XPS spectra of different catalysts, O 1s (a), Mn 2p (b) and Cu 2p (c).

Table 2 XPS surface composition analysis of different catalysts

	$Mn^{x+}/Mn^{[a]}$			$Cu^{x+}/Cu^{[b]}$	
Catalysts	Mn^{2+} (%)	Mn^{3+} (%)	Mn^{4+} (%)	Cu^{+} (%)	Cu^{2+} (%)
CuO				78.7	21.3
Cu2Mn1	23.3	65.4	11.2	23.6	76.4
Cu1Mn1	19.7	66.8	13.5	60.0	40.0
Cu1Mn2	14.2	68.0	17.7	69.6	30.4
MnO_δ	11.5	69.9	18.6		

[a] The whole Mn species with various valence states. [b] The whole Cu species with various valence states.

Table 3 Comparison of T_m' *vs.* O_{ads} proportion, and ΔT_m *vs.* Ω

Catalysts	$T_m'^{[a]}$ (°C)	$O_{ads}/(O_{ads} + O_{latt})^{[b]}$	$\Delta T_m^{[c]}$ (°C)	Ω
CuO	379	0.50		
Cu2Mn1	414	0.40	41	1.42
Cu1Mn1	397	0.49	73	2.14
Cu1Mn2	403	0.46	17	1.08
MnO_δ	413	0.43		

[a] T_m' is for the catalytic soot combustion in O_2/N_2 (Fig. S10). [b] O_{latt}: lattice oxygen. [c] $\Delta T_m = T_m' - T_m$, where T_m is for the catalytic soot combustion in $NO_x/O_2/N_2$ (Fig. 1a).

eqn (2)) to quantify the concentration of Cu^+–$Mn^{\lambda+}$ cation pair in different Cu*x*Mn*y* catalysts.

$$\Omega = \{(Cu^+/Cu)\cdot[Cu/(Cu + Mn)]\}/\{(Mn^{2+}/Mn)\cdot[Mn/(Cu + Mn)]\} \quad (2)$$

where, Cu (or Mn) stands for all the Cu (or Mn) species with different valence states, and all the atomic ratios are obtained by XPS measurement. The Ω values as well as the O_{ads} proportions for different catalysts are summarized in Table 3.

Catalytic activity measurement in the absence of NO_x (O_2/N_2) was also conducted in an attempt to find the key factors determining the catalysis performance. The catalytic behavior in O_2/N_2 (represented by T_m') was shown in Table 3. It's clearly observed that the higher ratio of $O_{ads}/(O_{ads} + O_{latt})$, the lower value of T_m' (the better catalytic activity), which is in good coincidence with the widely accepted "Active Oxygen Mechanism",[37] wherein soot is directly oxidized by the reactive oxygen species on catalyst surface. Additionally, it is worth noting that CuO with a slightly higher O_{ads} proportion than Cu1Mn1, possesses much better catalytic activity in O_2/N_2, indicating that the highest Cu^+ proportion in CuO could make extra contribution to its superb activity.

Additionally, a new parameter "ΔT_m" was introduced to quantify the enhancement efficiency of NO_x for catalytic activity of different Cu*x*Mn*y*, as shown in Table 3. It is interesting to find that Cu1Mn1 with the highest Ω value (2.14) shows the greatest NO_x enhancement efficiency (corresponding to the largest ΔT_m value of 73 °C), suggesting that in addition to "Active Oxygen Mechanism", the Cu^+–$Mn^{\lambda+}$ pairs as active sites could also promote the catalytic soot combustion by improving NO_2 production. Therefore, it is believed that the catalytic soot combustion in $NO_x/O_2/N_2$ over Cu1Mn1 follows both the "Active Oxygen Mechanism" and the "NO-aided Oxidation Mechanism".[37]

Mechanism analysis

Based on the above discussion, combined "Active Oxygen Mechanism" and "NO-aided Oxidation Mechanism" for catalytic soot combustion over Cu1Mn1 was proposed, as shown in Scheme 1. Therein, the "Active Oxygen Mechanism" shown in

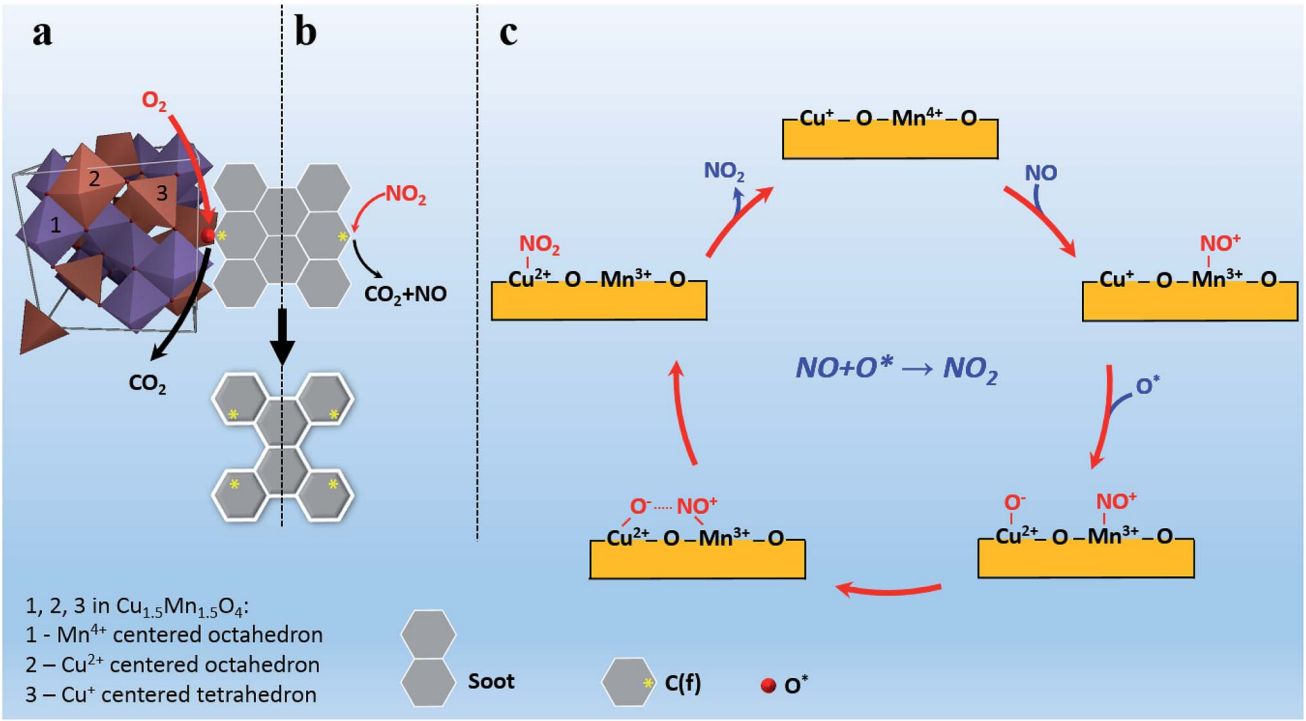

Scheme 1 Schematic illustrations of the possible combined catalytic mechanism, (a) "Active Oxygen Mechanism", (b) "NO-aided Oxidation Mechanism", (c) formation of NO_2 in the "NO-aided Oxidation Mechanism".

Scheme 1a indicates that the active oxygen species (O*) can attack the nearby active sites on carbon surface [C(f)], producing carbon oxides (mostly CO_2) and more C(f) (eqn (3)).[38] Afterwards, the spent oxygen species can be supplemented by gaseous O_2.[37]

$$2O^* + CCC(f) \rightarrow CO_2 + 2C(f) \quad (3)$$

Scheme 1b shows the schematic illustration of "NO-aided oxidation mechanism". Similar to O* in the "Active Oxygen Mechanism", NO_2 can also directly oxidize C(f) into CO_2, and regenerate more C(f) (eqn (4)).[39] The process of NO_2 production over Cu^+–$Mn^{\lambda+}$ cation pairs (herein, Cu^+–Mn^{4+} is taken as an example) is depicted in Scheme 1c.

$$2NO_2 + CCC(f) \rightarrow 2NO + CO_2 + 2C(f) \quad (4)$$

$$Cu^+ + 1/2O_2 \rightarrow Cu^{2+}\cdot O^- \quad (5)$$

$$Mn^{4+} + NO \rightarrow Mn^{3+}\cdot NO^+ \quad (6)$$

$$Cu^{2+}\cdot O^- + Mn^{3+}\cdot NO^+ \rightarrow Cu^{2+}\cdot NO_2 + Mn^{3+} \quad (7)$$

$$Cu^{2+}\cdot NO_2 \rightarrow Cu^{2+} + NO_2(g) \quad (8)$$

Cu^+ cations in $Cu_{1.5}Mn_{1.5}O_4$ can adsorb, then activate gaseous O_2 to generate active oxygen (eqn (5)).[35] Similarly, $Mn^{\lambda+}$ cations can also adsorb as well as activate NO in the feed gas, resulting in reactive nitrogen oxide (NO^+) species (eqn (6)).[36] Then, the produced active species can easily react with each other to form NO_2, as shown in eqn (7).[36] The obtained NO_2, as a stronger oxidant than O_2,[40] can effectively accelerate soot combustion (Fig. S11†). Besides, it is worth noting that the NO_2 molecules are inclined to adsorb on metal ions, *e.g.*, Cu^{2+}, producing $Cu^{2+}\cdot NO_2$ species.[41]

The presence of such $Cu^{2+}\cdot NO_2$ species could keep NO_2 from effusion into the gas flow at low temperatures, and ensure the steady release of NO_2 when heated (eqn (8)), thus realizing the full use of NO_2. This can well explain the finding that MnO_δ, though with the higher NO_2 producing activity than Cu1Mn1 (Fig. S12†), shows lower enhancement efficiency of NO_x for catalytic soot combustion, especially in high temperatures (Fig. S13†). After NO_2 releasing, the active sites can be regenerated through reaction equilibrium $Mn^{3+} + Cu^{2+} \leftrightarrow Cu^+ + Mn^{4+}$, thus completing the catalysis circle.

To sum it up, the presence of enormous O_{ads} and Cu^+–$Mn^{\lambda+}$ cation pairs on Cu1Mn1 surface mainly contributes to the extremely high intrinsic catalytic activity of the spinel $Cu_{1.5}Mn_{1.5}O_4$ phase, and the interaction between NO_2 and Cu^{2+} also ensures the sufficient utilization of NO_2.

In Situ DRIFT studies of soot combustion over Cu1Mn1

To verify the mechanism shown in Scheme 1, DRIFT measurement was performed to investigate the existence and evolution of different types of absorbed species over Cu1Mn1 during catalytic soot oxidation in $NO_x/O_2/N_2$, as shown in Fig. 5. It is clearly found that the intensity of the NO_2^- peak *ca.* 1250 cm^{-1} decreases with increasing temperatures (RT-400 °C),[42] and NO_3^- peak *ca.* 1404 cm^{-1} can be obviously observed at 400 °C.[43] The

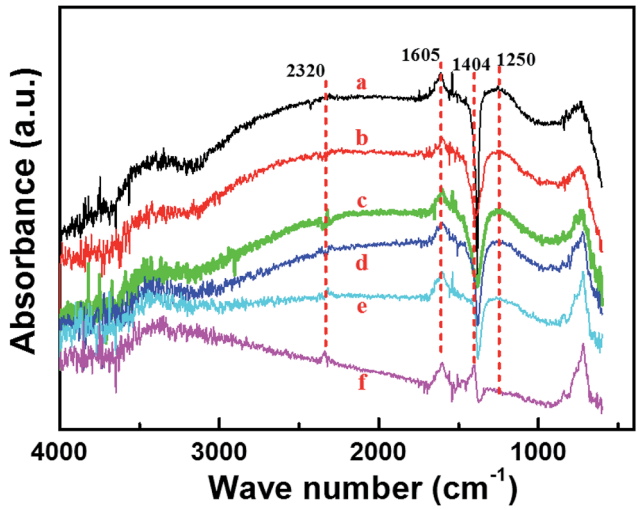

Fig. 5 *In situ* DRIFT spectra during the catalytic soot combustion on Cu1Mn1 ((a) RT, (b) 100 °C, (c) 200 °C, (d) 300 °C, (e) 350 °C, (f) 400 °C). Feed gas: N_2 (balance) + O_2 (10%) + NO (350 ppm).

evolution of the NO_2^- peak and the appearence of the NO_3^- peak both indicate the gradual oxidation of NO_x species on the catalyst surface with increasing temperature. In addition, the presence of both NO^+ (~2320 cm^{-1})[44] and the $Cu^{2+}\cdot NO_2$ intermediates (~1605 cm^{-1})[42] is also confirmed by the spectra.

Conclusions

A facile co-precipitation method was utilized to prepare a series of Cu*x*Mn*y* oxides to catalyze the combustion of diesel soot in $NO_x/O_2/N_2$. Among, Cu1Mn1 with a pure phase of spinel-type $Cu_{1.5}Mn_{1.5}O_4$, shows the optimized catalytic activity (T_f = 360 °C, under loose contact mode), owing to both its beneficial morphological features and high intrinsic activity. The well-dispersed rough microspheres in Cu1Mn1 could facilitate soot combustion by improving the contact between soot and the active sites on catalyst surface. Besides, the presence of stacked pores among the loosely-packed nanoparticles within the microspheres is also helpful for the diffusion of gaseous reactant or product, such as O_2, NO and NO_2. Apart from these beneficial morphological features, the pure spinel $Cu_{1.5}Mn_{1.5}O_4$ in Cu1Mn1, as highly active phase, could provide abundant O_{ads} and Cu^+–$Mn^{\lambda+}$ cation pairs, as well as Cu^{2+}–NO_2 interaction. The reactive O_{ads} could directly oxidize soot following the "Active Oxygen Mechanism". And the Cu^+–$Mn^{\lambda+}$ cation pairs could accelerate production of NO_2, which, by virtue of Cu^{2+}–NO_2 interaction, will effectively enhance soot combustion following the "NO-aided Oxidation Mechanism". This kind of Cu*x*Mn*y* mixed oxides prepared by this low-cost and easily-scalable method may find its potential application in the catalytic removal of soot in the diesel exhaust.

Acknowledgements

This research was sponsored by National Key Basic Research Program of China (2013CB933202), China National Funds for Distinguished Young Scientists (51225202) and National Natural Science Foundation of China (51502330).

Notes and references

1 B. A. Van Setten, M. Makkee and J. A. Moulijn, *Catal. Rev.*, 2001, **43**, 489–564.
2 H. Horvath, *Atmos. Environ.*, 1993, **27**, 293–317.
3 X. Yu, Z. Zhao, Y. Wei, J. Liu, J. Li, A. Duan and G. Jiang, *Chin. J. Catal.*, 2015, **36**, 1957–1967.
4 E. Obeid, L. Lizarraga, M. Tsampas, A. Cordier, A. Boréave, M. Steil, G. Blanchard, K. Pajot and P. Vernoux, *J. Catal.*, 2014, **309**, 87–96.
5 J. O. Uchisawa, A. Obuchi, Z. Zhao and S. Kushiyama, *Appl. Catal., B*, 1998, **18**, L183–L187.
6 X. Wu, S. Liu, F. Lin and D. Weng, *J. Hazard. Mater.*, 2010, **181**, 722–728.
7 J. Xu, J. Liu, Z. Zhao, C. Xu, J. Zheng, A. Duan and G. Jiang, *J. Catal.*, 2011, **282**, 1–12.
8 D. Fino, N. Russo, G. Saracco and V. Specchia, *J. Catal.*, 2006, **242**, 38–47.
9 L. Castoldi, R. Matarrese, L. Lietti and P. Forzatti, *Appl. Catal., B*, 2009, **90**, 278–285.
10 J. Liu, Z. Zhao, J. Wang, C. Xu, A. Duan, G. Jiang and Q. Yang, *Appl. Catal., B*, 2008, **84**, 185–195.
11 Y. Wei, J. Liu, Z. Zhao, A. Duan, G. Jiang, C. Xu, J. Gao, H. He and X. Wang, *Energy Environ. Sci.*, 2011, **4**, 2959–2970.
12 L. Nascimento, J. Lima, P. de Sousa Filho and O. Serra, *Chem. Eng. J.*, 2016, **290**, 454–464.
13 Y. Nagahara, S. Sugawara and K. Shinohara, *J. Power Sources*, 2008, **182**, 422–428.
14 I. Heo, J. W. Choung, P. S. Kim, I.-S. Nam, Y. I. Song, C. B. In and G. K. Yeo, *Appl. Catal., B*, 2009, **92**, 114–125.
15 S. Behar, N.-A. Gomez-Mendoza, M.-A. Gomez-Garcia, D. Swierczynski, F. Quignard and N. Tanchoux, *Appl. Catal., A*, 2015, **504**, 203–210.
16 J. Papavasiliou, G. Avgouropoulos and T. Ioannides, *J. Catal.*, 2007, **251**, 7–20.
17 Y. Tanaka, T. Utaka, R. Kikuchi, T. Takeguchi, K. Sasaki and K. Eguchi, *J. Catal.*, 2003, **215**, 271–278.
18 I. Spassova, M. Khristova, D. Panayotov and D. Mehandjiev, *J. Catal.*, 1999, **185**, 43–57.
19 A. S. Reddy, C. S. Gopinath and S. Chilukuri, *J. Catal.*, 2006, **243**, 278–291.
20 P. Decyk, A. B. Więckowski, L. Najder-Kozdrowska, I. Bilkova and M. Ziolek, *Copper and manganese mixed oxides in zeolites: study of EMR spectra*, ed. C. Rudowicz, Z. Sojka, J. Jezierska and P. Pietrzyk, Polish EMR Group, Krakow, 2014.
21 R. Vandenberghe, E. Legrand, D. Scheerlinck and V. Brabers, *Acta Crystallogr., Sect. B: Struct. Crystallogr. Cryst. Chem.*, 1976, **32**, 2796–2798.
22 R. Bayon, G. S. Vicente, C. Maffiotte and A. Morales, *Sol. Energy Mater. Sol. Cells*, 2008, **92**, 1211–1216.
23 X. Zhou, H. Chen, G. Zhang, J. Wang, Z. Xie, Z. Hua, L. Zhang and J. Shi, *J. Mater. Chem. A*, 2015, **3**, 9745–9753.
24 L. Cai, Z. Hu, P. Branton and W. Li, *Chin. J. Catal.*, 2014, **35**, 159–167.

25 A. L. Kustov and M. Makkee, *Appl. Catal., B*, 2009, **88**, 263–271.
26 B. Dernaika and D. Uner, *Appl. Catal., B*, 2003, **40**, 219–229.
27 S. Xie, Y. Liu, J. Deng, X. Zhao, J. Yang, K. Zhang, Z. Han and H. Dai, *J. Catal.*, 2016, **342**, 17–26.
28 U. Ilyas, R. Rawat, G. Roshan, T. Tan, P. Lee, S. Springham, S. Zhang, L. Fengji, R. Chen and H. Sun, *Appl. Surf. Sci.*, 2011, **258**, 890–897.
29 M. Kang, E. D. Park, J. M. Kim and J. E. Yie, *Appl. Catal., A*, 2007, **327**, 261–269.
30 R. Sun, L. Wang, H. Yu, A. Zain ul, Y. Chen, H. Khalid, N. M. Abbasi, M. Akram, S. Z. Vatsadze and D. A. Lemenovskii, *J. Inorg. Organomet. Polym.*, 2016, **26**, 545–554.
31 P. E. Laibinis and G. M. Whitesides, *J. Am. Chem. Soc.*, 1992, **114**, 9022–9028.
32 Y. Tanaka, T. Takeguchi, R. Kikuchi and K. Eguchi, *Appl. Catal., A*, 2005, **279**, 59–66.
33 Y. Maimaiti, M. Nolan and S. D. Elliott, *Phys. Chem. Chem. Phys.*, 2014, **16**, 3036–3046.
34 Z. Li, M. Meng, F. Dai, T. Hu, Y. Xie and J. Zhang, *Fuel*, 2012, **93**, 606–610.
35 J. Sarkany, *J. Mol. Struct.*, 1997, **410**, 95–98.
36 J. Wang, J. Zhu, X. Zhou, Y. Du, W. Huang, J. Liu, W. Zhang, J. Shi and H. Chen, *J. Mater. Chem. A*, 2015, **3**, 7631–7638.
37 A. Bueno-López, *Appl. Catal., B*, 2014, **146**, 1–11.
38 W. Shangguan, Y. Teraoka and S. Kagawa, *Appl. Catal., B*, 1997, **12**, 237–247.
39 M. Jeguirim, V. Tschamber, K. Villani, J. F. Brilhac and J. A. Martens, *Chem. Eng. Technol.*, 2009, **32**, 830–834.
40 A. Setiabudi, M. Makkee and J. A. Moulijn, *Appl. Catal., B*, 2004, **50**, 185–194.
41 Y. Li, J. Liang, Z. Tao and J. Chen, *Mater. Res. Bull.*, 2008, **43**, 2380–2385.
42 R. Izquierdo, L. J. Rodriguez, R. Anez and A. Sierraalta, *J. Mol. Catal. A: Chem.*, 2011, **348**, 55–62.
43 U. Bentrup, A. Brückner, M. Richter and R. Fricke, *Appl. Catal., B*, 2001, **32**, 229–241.
44 K. I. Hadjiivanov, *Catal. Rev.*, 2000, **42**, 71–144.